Supporting Information

A Numerical Study of the Photothermal Behaviour of Near-Infrared Plasmonic Colloids

Kai Liu[1], Xiaozheng Xue[2], and Edward P. Furlani[1,2,*]

[1]Dept. of Electrical Engineering, University at Buffalo SUNY, NY 14260

[2]Dept. of Chemical and Biological Engineering, University at Buffalo SUNY, NY 14260

Computational Domain

In the computational domain, a single colloidal particle is centered at the origin of the domain and immersed in H_2O. The particle is illuminated with a uniform downward-directed plane wave with the E field polarized along the x-axis. The height of the CD is 1000 nm and perfectly matched layers (PMLs) (200 nm in height) are applied at the top and bottom of the domain to reduce backscatter from these boundaries. Perfect electric conductor (PEC) conditions are applied at the boundaries perpendicular to E, and perfect magnetic conductor (PMC) conditions are applied at the boundaries perpendicular to H.

We use full-wave time harmonic field theory for the analysis. The time-harmonic E field within the domain satisfies the equation:

$$\nabla \times \left(\mu_r^{-1} \nabla \times \mathbf{E}\right) - k_0^2 \left(\varepsilon_r - j\frac{\sigma}{\omega \varepsilon_0}\right)\mathbf{E} = 0 \qquad \text{(S1)}$$

where μ_r, ε_r and σ are the relative permeability, permittivity and conductivity of the media, respectively.

In order to simultaneously guarantee the accuracy of the solution and maintain reasonable computational burden, we assigned at least 5 layers of meshes for the critical geometric features. For example, for the Au shell with the thickness of t_s, we assigned the maximum mesh size as $t_s/5$. We also assigned the maximum mesh size as $W/5$ for the Au nanocage, wherein W is the width of the each constituent nanowire. In terms of the uniform background which has a less complex optical and thermal interaction, its mesh will gradually grow based on the mesh imposed on the critical features of the nanoparticles with a growth rate of 1.2.

Material Properties

To model the nanoparticles, we need expressions for optical constants $\varepsilon_r = (n\text{-}ik)^2$ of Au (ε_{Au}), SiO_2 (n_{SiO2}) and the background medium (n_{H2O}). Moreover, we need to consider the fact that the metallic materials (e.g. Au shell) can be thinner than the mean free path of free electrons (~ 42 nm). A dielectric function for gold that accounts for electron-surface scattering is expressed in **eqn (S2)**[1]

$$\varepsilon_{Au}\left(\omega, L_{eff}\right) = \varepsilon_{Au,bulk}\left(\omega\right) + \frac{\omega_p^2}{\omega^2 + i\omega v_f / l_\infty} - \frac{\omega_p^2}{\omega^2 + i\omega\left(v_f / l_\infty + A v_f / L_{eff}\right)} \qquad \text{(S2)}$$

where $\varepsilon_{Au,bulk}$ is the bulk dielectric function of gold, ω is the angular frequency of incident light, $\omega_p = 0.93$ eV is the plasma frequency, $vf = 1.4 \times 1015$ nm/s is the Fermi velocity, $l\infty = 42$ nm is the mean free path of the free electrons, A is a dimensionless parameter, usually assumed to be close to unity ($A = 1$) and $L_{eff} = t_s$ is the reduced effective mean free path of the free electrons. The bulk dielectric function is given by an analytical expression **eqn (S3)** that is based on an experiment-fitted critical points model.[2-4] The detailed descriptions of parameters in **eqn (S3)** can be found in the literature.[2-4] The material SiO_2 is assumed to be lossless, i.e. $k_{SiO2} = 0$, with a dispersive index of refraction defined in **eqn (S4)**.[1] The refractive index of the nonabsorbing water surrounding is expressed in **eqn (S5)**.[1] Moreover, all materials in our model have the permeability of $\mu_r = 1$.

$$\varepsilon_{Au,bulk}(\lambda) = \varepsilon_\infty - \frac{1}{\lambda_p^2\left(\frac{1}{\lambda^2} - i\frac{1}{\gamma_p\lambda}\right)} + \sum_{n=1,2}\frac{A_n}{\lambda_n}\left[\frac{e^{i\phi_n}}{\left(\frac{1}{\lambda_n} - \frac{1}{\lambda} + i\frac{1}{\gamma_n}\right)} + \frac{e^{-i\phi_n}}{\left(\frac{1}{\lambda_n} + \frac{1}{\lambda} - i\frac{1}{\gamma_n}\right)}\right] \quad \text{(S3)}$$

$$n_{SiO_2}^2 = 1 + \frac{0.6961663\lambda^2}{\lambda^2 - (0.0684043)^2} + \frac{0.4079426\lambda^2}{\lambda^2 - (0.1162414)^2} + \frac{0.8974794\lambda^2}{\lambda^2 - (9.896161)^2} \quad \text{(S4)}$$

$$n_{H_2O}^2 = 1 + \frac{0.5684027565\lambda^2}{\lambda^2 - 0.005101829712} + \frac{0.1726177391\lambda^2}{\lambda^2 - 0.01821153936} + \frac{0.02086189678\lambda^2}{\lambda^2 - 0.02620722293} + \frac{0.1130748688\lambda^2}{\lambda^2 - 10.69792721} \quad \text{(S5)}$$

Mie Theory

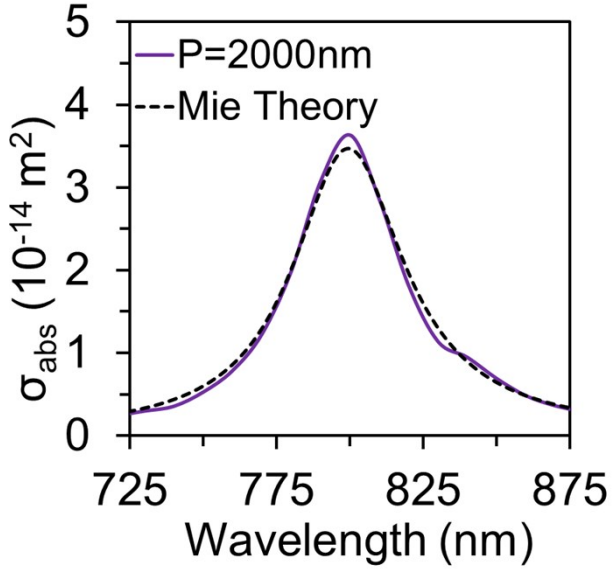

Fig. S1 Comparison of absorption cross sections of the SiO_2@Au colloid with R_c = 27.3 nm and t_s = 3.7 nm based on FE-based solution and Mie theory prediction.

We use Mie theory to predict the optical absorption of core-shell plasmonic particles as a function of the incident wavelength. The extinction, scattering and absorption efficiencies k_{ext}, k_{scat} and k_{abs} for the particles are computed using

$$k_{ext} = \frac{2}{\alpha_1^2}\sum_{n=1}^{\infty}(2n+1)\mathrm{Re}(a_n + b_n) \tag{S6}$$

$$k_{scat} = \frac{2}{\alpha_1^2}\sum_{n=1}^{\infty}(2n+1)\left(|a_n|^2 + |b_n|^2\right) \tag{S7}$$

$$k_{abs} = k_{ext} - k_{scat} \tag{S8}$$

where a_n and b_n are scattering coefficients taken from Bohren and Huffman (1983)[5], i.e.,

$$\begin{aligned} a_n &= \frac{\psi_n(\alpha_1)\left[\psi_n'(m_1\alpha_1) - A_n\chi_n'(m_1\alpha_1)\right] - m_1\psi_n'(\alpha_1)\left[\psi_n(m_1\alpha_1) - A_n\chi_n(m_1\alpha_1)\right]}{\zeta_n(\alpha_1)\left[\psi_n'(m_1\alpha_1) - A_n\chi_n'(m_1\alpha_1)\right] - m_1\zeta_n'(\alpha_1)\left[\psi_n(m_1\alpha_1) - A_n\chi_n(m_1\alpha_1)\right]} \\ b_n &= \frac{m_1\psi_n(\alpha_1)\left[\psi_n'(m_1\alpha_1) - B_n\chi_n'(m_1\alpha_1)\right] - \psi_n'(\alpha_1)\left[\psi_n(m_1\alpha_1) - B_n\chi_n(m_1\alpha_1)\right]}{m_1\zeta_n(\alpha_1)\left[\psi_n'(m_1\alpha_1) - B_n\chi_n'(m_1\alpha_1)\right] - \zeta_n'(\alpha_1)\left[\psi_n(m_1\alpha_1) - B_n\chi_n(m_1\alpha_1)\right]} \end{aligned} \tag{S9}$$

with

$$\begin{aligned} A_n &= \frac{m_1\psi_n(m_1\alpha_2)\psi_n'(m_2\alpha_2) - m_2\psi_n'(m_1\alpha_2)\psi_n(m_2\alpha_2)}{m_1\chi_n(m_1\alpha_2)\psi_n'(m_2\alpha_2) - m_2\chi_n'(m_1\alpha_2)\psi_n(m_2\alpha_2)} \\ B_n &= \frac{m_1\psi_n(m_2\alpha_2)\psi_n'(m_1\alpha_2) - m_2\psi_n'(m_2\alpha_2)\psi_n(m_1\alpha_2)}{m_1\chi_n'(m_1\alpha_2)\psi_n(m_2\alpha_2) - m_2\chi_n(m_1\alpha_2)\psi_n'(m_2\alpha_2)} \end{aligned} \tag{S10}$$

and

$$m_1 = \frac{n_1}{n_m} \quad \alpha_1 = \frac{2\pi R_1 n_m}{\lambda} \quad m_2 = \frac{n_2}{n_m} \quad \alpha_2 = \frac{2\pi R_2 n_m}{\lambda} \tag{S11}$$

Here $R_1 = t_s + R_c$ is the radius of the core-shell particle, n_1 is the refractive index of the shell. $R_2 = R_c$ and n_2 are the radius and refractive index of the core, respectively. n_m is the refractive index of the surrounding medium (carrier fluid), which throughout this work is assumed to be H_2O. The functions ψ_n, χ_n, ζ_n are Riccati–Bessel functions, which can be expressed as

$$\psi_n(z) = \sqrt{\frac{\pi z}{2}}J_{n+(1/2)}(z), \qquad \chi_n(z) = -\sqrt{\frac{\pi z}{2}}N_{n+(1/2)}(z), \qquad \zeta_n(z) = \sqrt{\frac{\pi z}{2}}H^{(2)}_{n+(1/2)}(z) \tag{S12}$$

where $J_{n+(1/2)}$, $N_{n+(1/2)}$ represent, respectively, half integer-order Bessel functions of the first and second kind and $H^{(2)}_{n+(1/2)}$ represents the half-integer-order Hankel function of the second kind. The extinction, scattering and absorption cross-sections of a particle, σ_{ext}, σ_{scat} and σ_{abs}, are just the product of the corresponding efficiency times the geometric cross-sectional area A_p e.g., $\sigma_{abs} = k_{abs}\cdot A_p = k_{abs}\cdot(\pi(t_s + R_c)^2)$ (m^2).

When we observed curves shown in **Fig. S1**, we found a similar peak on the shoulder of the curve based on the simulation result. On the other hand, the curve based on Mie theory does not possess this

feature. In this case, this difference is attributed to the remaining diffractive coupling between neighboring particles. Though we largely decouple the interaction between particles, a very slight long-range diffractive coupling still remains. However, this existing coupling won't necessarily perturb the amplitude and wavelength of the main absorption peak.

Field Comparison

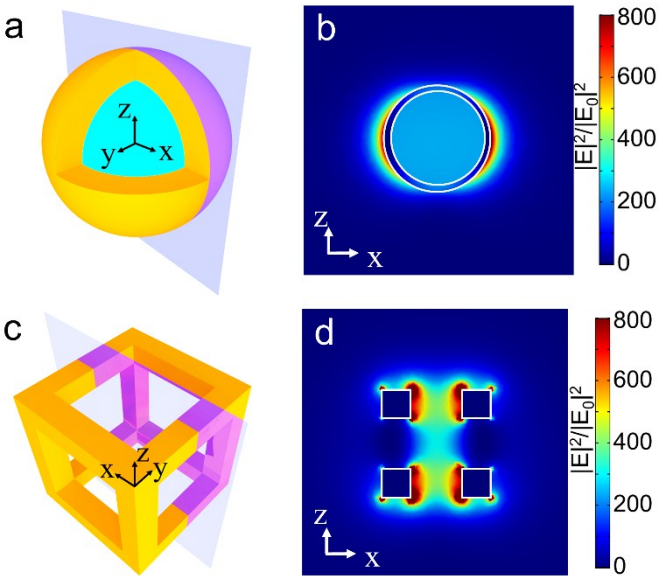

Fig. S2 (a) and (c) The conceptual schmatics showing the designated planes for field plots. (b) and (d) Local field enhancement profiles of the core-shell and Au nanocage at the LSPR wavelength of 800 nm. The direction of the linear incident polarization is along x-axis and the direction of light propagation is along the negative direction of z-axis.

In **Fig. S2**, we plot the spatial profile of E field intensity enhancement ($|\mathbf{E}|^2/|\mathbf{E_0}|^2$) for the SiO_2@Au core-shell and Au nanocage particles. **Fig. S2a** and **S2c** illustrate xz-planes for field plots of two particles which are parallel to the polarization. Both planes cut through the centers of the particles. In terms of the core-shell particle, its field enhancement profile reveals a typical dipolar resonance, as shown in **Fig. S2b**. However, the Au nanocage possesses an advantage over the core-shell because of the additional strong mode coupling in the hollow interior, as shown in **Fig. S2d**. Because of the strong coupling among nanowire frames of the nanocage, the enhancement effect is much stronger as compared with the core-shell. Therefore, the Au nanocage provides a better platform for theranostic applications.

References

1. P. Tuersun and X. Han, *Appl. Opt.*, 2013, **52**, 1325-1329.
2. P. G. Etchegoin, E. C. Le Ru and M. Meyer, *J. Chem. Phys.*, 2006, **125**, 164705.
3. P. G. Etchegoin, E. C. Le Ru and M. Meyer, *J. Chem. Phys.*, 2007, **127**, 189901-189901-189901.
4. P. B. Johnson and R. W. Christy, *Phys. Rev. B* 1972, **6**, 4370-4379.
5. C. F. Bohren and D. R. Huffman, *Absorption and Scattering of Light by Small Particles*, Wiley, New York, 1983.